

Tunable transverse optical radiation forces induced by hybridization of electric and magnetic modes

WeiQi Deng ¹, Xiangshi Kong,¹ Haitao Xu,^{1,2} Yongbing Long,^{1,2} and Haidong Deng ^{1,2,*}

¹College of Electronic Engineering, South China Agricultural University, Guangzhou 510642, China

²Guangdong Laboratory of Lingnan Modern Agriculture, Guangzhou 510642, China



(Received 30 September 2023; accepted 12 February 2024; published 1 March 2024)

Transverse radiation forces acting on the silicon nanoparticles illuminated by a tightly focused laser beam are investigated by using the Maxwell stress-tensor method combined with generalized Lorenz-Mie theory. It is found that the radiation force can be tuned flexibly by electric–magnetic multipolar resonances and the hybridization of the both kinds of resonances, and the nanoparticle receives a negative or positive transverse radiation force. We also analyze theoretically the far-field scattering patterns and the contributions of each typical electric–magnetic resonance and hybridization of electric and magnetic modes to the radiation forces on silicon nanoparticles with the multipolar expansion method. The simulation research results show that the negative (positive) transverse radiation forces mainly originate from the asymmetric far-field scattering when the particles are positioned at different positions in the focus plane. Our findings cannot only provide an effective strategy to enhance the efficiency of optical trapping of nanoparticles with the excitation of electric–magnetic resonances but also facilitate the optical sorting, selective trapping, and assembling of nanoparticles with a single tightly focused laser beam.

DOI: [10.1103/PhysRevA.109.033501](https://doi.org/10.1103/PhysRevA.109.033501)

I. INTRODUCTION

Optical tweezers have been widely used in biology [1,2], biochemistry [3–5], and physics [6–8] because of the desirable capability of remote and noninvasive trapping and manipulation of mesoscopic nanoobjects since the radiation force was first applied to accelerate and trap macroscopic dielectric spheres by Ashkin in the 1970s [9]. In recent years, the trapping abilities of optical tweezers have extended from micrometer to nanometer scale with the advances of nanotechnology [10,11]. However, trapping and manipulation of a nano-object with single tightly focused laser beam still remains greatly challenging due to the diffraction-limited trapping volume [12]. Compared to nonresonant nanoparticles (polystyrene and glass nanoparticles) in the visible region, resonant nanoparticles such as plasmonic nanoparticles and high refractive index nanoparticles, have been experimentally and theoretically proved much easier to be trapped and manipulated by enhancing the interaction between nanoparticles and the focused laser beam [13–16]. For the former, a typical case is that some plasmonic nanorods can be effectively trapped and manipulated by a single focused laser beam with the excitation of the localized surface plasmonic resonance [17,18]. Interestingly, the trapped nanorods can be aligned and rotated by tuning the polarization directions of the trapping laser beam due to dominant nonconservative force exerted on the gold nanorods [19], which is a consequence of the polarization-dependent surface plasmonic resonance and very different from the optical gradient force. Z. Li *et al.* theoretically demonstrated that the polarization-dependent optical

force can be enhanced up to $2.7\times$ contrast to the gradient force because of the excitation of Fano resonance in plasmonic nanoparticles [20]. Based on these researches, a new strategy for selectively trapping nanoparticles was proposed by exciting the resonances of the trapped nano-objects.

For the latter, as a competitive alternative to plasmonic nanoparticles, dielectric nanoparticles with high refractive index have attracted great interest during the past several years for supporting electric and magnetic resonances from the near ultraviolet to near infrared with almost no dissipative losses [21–23]. The desirable overlapping of multipolar resonant modes of these nanoparticles can be used for a variety of applications such as sensors [24], surface enhanced Raman detections [25], and energy-harvesting technology [26]. Recently, selectively optical trapping and controlled printing of silicon nanoparticles under the excitation of optical resonance have been experimentally demonstrated in the silicon colloid [27], which has been proven to be an alternative for fabrication of ordered nanoantenna arrays and multifunctional metasurfaces for these applications mentioned above. Therefore, in order to realize the precise trapping and controllable printing of silicon nanoparticles, it is of paramount important to investigate theoretically the optomechanics of silicon nanoparticles in the optical trap. Most recently, the directional scattering and multipolar contributions to optical forces on silicon nanoparticles were investigated by using the transfer matrix method [28]. However, only effects of electric and magnetic dipolar resonance on the axial radiation forces have been considered in that paper [28].

In this work, we investigate the contributions of multipolar resonances (up to the third order) and interferences between multipolar resonances to transverse optical radiation forces acting on silicon nanoparticles illuminated by a single focused

*Corresponding author: dhdong@scau.edu.cn

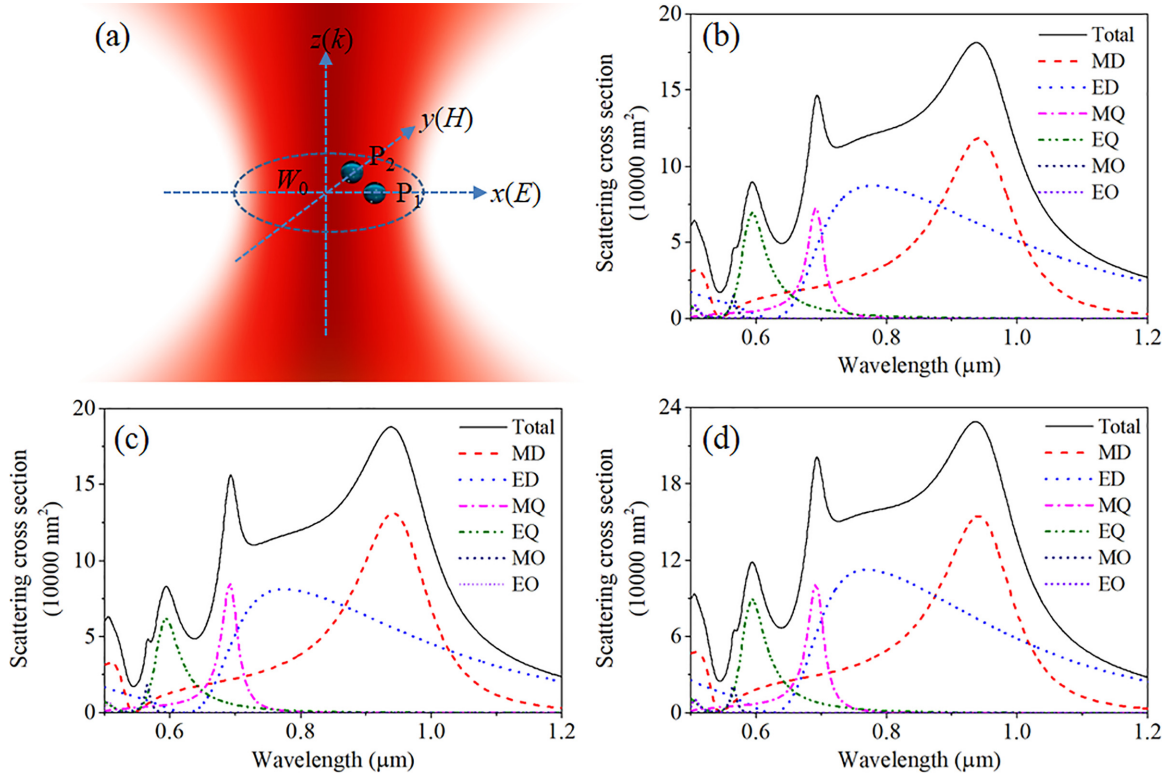


FIG. 1. (a) Schematic showing the Si nanoparticle excited with a focused linearly polarized Gaussian beam. The focused linearly polarized Gaussian beam illuminates the Si nanoparticles along with $+z$ direction and the directions of electric and magnetic fields are along with x and y directions, respectively. Spectra of scattering cross section and corresponding multipolar decomposition when the silicon nanoparticle is positioned at P_1 (b) and P_2 (c). (d) Spectrum of scattering cross section and corresponding multipoles' contributions when the same silicon nanoparticle is illuminated by a plane EM wave.

laser beam with the Maxwell stress-tensor (MST) combined with the generalized Lorenz-Mie theory (GLMT) approaches. First, the scattering spectra and the contributions of multipolar resonances of silicon nanoparticles located at different positions in the focus plane of the Gaussian beam are examined with GLMT [29]. Second, the total transverse radiation forces exerted on the silicon nanoparticles and the decompositions of the total optical forces corresponding to the contributions of each resonance and interference between adjacent multipolar resonances can be calculated by integrating all the scattering components of multipolar resonant modes by using the MST approach [30–32]. In contrast to previous work, a kind of magnetic polarization-dependent optical transverse radiation force, as the counterpart of electric polarization-dependent optical transverse forces, is demonstrated by investigating the evolution of the optical radiation force when the nanoparticles are put in electric and magnetic polarization directions, respectively. Finally, to understand the underlying physics, we also observe the far-field scattering patterns including the forward, backward, and side scatterings as the nanoparticles are positioned in the corresponding locations in the focus plane.

II. RESULTS AND DISCUSSION

In this paper we only consider the transverse optical radiation forces acting on the silicon nanoparticles located in the focus plane of the Gaussian beam, as shown in Fig. 1(a).

The beam-waist radius W_0 of the Gaussian beam is set to be $0.5 \mu\text{m}$. The incident power is set to be 10 mW. The dielectric permittivity of silicon was taken from a textbook (Ref. [33]). All calculations were performed assuming a homogeneous aqueous surrounding medium ($n_s = 1.33$).

In order to investigate the effect of the single electric (magnetic) resonance on the scattering and the transverse optical force, we start from the multipolar decomposition of the scattering spectrum when a silicon nanoparticle with radius of $R = 125 \text{ nm}$ is positioned at $x = W_0/2, y = 0, z = 0$ (marked as P_1) and $x = 0, y = W_0/2, z = 0$ (marked as P_2), respectively. For comparison, the multipolar decomposition of the scattering spectrum of the same sized silicon nanoparticles illuminated by a plane electromagnetic wave is also provided, as shown in Fig. 1(d). One can see that besides the dipolar modes, the higher-order multipolar resonances are excited with the decreasing of the light wavelength. It should be mentioned here that we only provide multipolar resonances up to third order and neglect the higher-order resonances because of the weak resonant response in the considered wavelength range. To contrast with the case that the silicon nanoparticles are excited with a plane electromagnetic wave, as shown in Fig. 1(d), it can be seen clearly that the resonant peak of each mode remains unchanged as the silicon nanoparticle is placed in both positions, while the contributions from the electric and magnetic multipolar resonances to the total scattering spectrum are totally different from each other. Close inspections of Figs. 1(b) and 1(c) show that a polarization-dependent

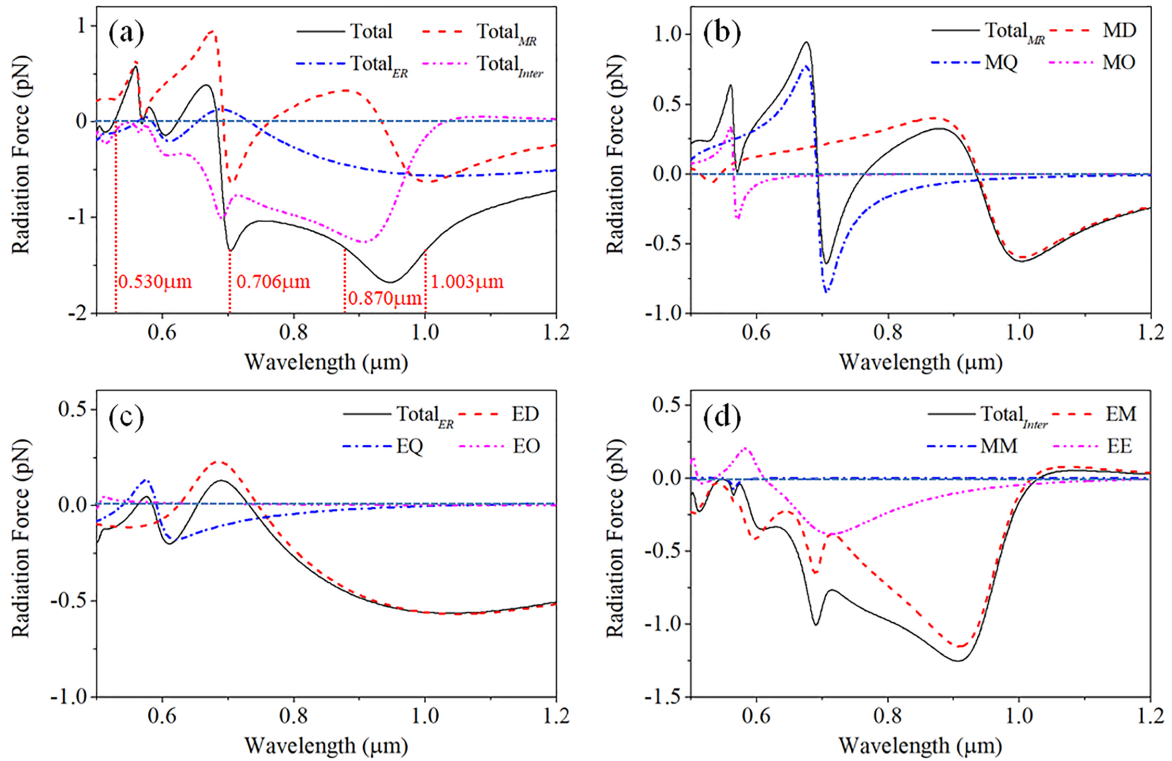


FIG. 2. The total transverse radiation force and the corresponding decomposition when the Si nanoparticle is placed at P_1 . (a) The total transverse radiation force and the contributions from the magnetic (total_{MR}) and electric (total_{ER}) multipoles and interferences of both modes (total_{inter}). The red dotted lines indicate the wavelengths, for which the far-field patterns are presented in Fig. 5. (b) The contribution from the magnetic multipoles and the corresponding decomposition (MD, MQ, and MO). (c) The contribution from the electric multipoles and the corresponding decomposition (ED, EQ, and EO). (d) The contribution from the interference of both kinds of modes and the corresponding decomposition (EM, MM, and EE).

contribution to the scattering intensity can be realized when the silicon nanoparticle is positioned in the electric- and magnetic-field directions. It can be seen that the electric multipolar resonances provide more contributions to the total scattering spectrum as the silicon nanoparticle is positioned at P_1 than that of the case when the silicon nanoparticle is placed at P_2 . Similarly, when the silicon nanoparticle is located at P_2 the contributions to the total scattering from the magnetic multipole resonance can be improved correspondingly. Therefore, Fig. 1(b) displays that the electric quadrupole (EQ) resonance provides almost the same contribution to the scattering cross section as that of the magnetic quadrupole (MQ) resonance. Similarly, this effect is also manifested in Fig. 1(c), where the scattering contribution from the MQ is larger than that of the EQ, and even larger than that of the electric dipole resonance mode (ED).

From Eq. (A7) in the Appendix, we can see that the contribution of each resonance to scattering is mainly dominated by not only the Mie scattering coefficients a_n and b_n but also the beam-shaped coefficients a_{mn}^i and b_{mn}^i . The former determines the resonant peaks in the considered wavelength range. Hence, we can see from Figs. 1(b) and 1(c) that all these multipolar resonant peaks for the case of excitation with a Gaussian beam are similar to that of the case of excitation with a plane electromagnetic wave [see Fig. 1(d)]. However, the latter corresponding to the geometric characters of the focused plane can tune the relative strength of each

multipolar resonance when the nanoparticles are placed in different positions in the focused laser beam. Therefore, the relative scattering strength of electric–magnetic multipole resonances can be selectively enhanced or suppressed when the silicon nanoparticle is placed in the electric–magnetic polarization direction.

In this section the transverse radiation forces are considered when a silicon nanoparticle is located in the focus plane of Gaussian beam. We first consider two typical cases mentioned in the Sec. II that the silicon nanoparticle is placed at P_1 and P_2 , respectively. Figure 2(a) presents the total transverse radiation force spectra and the total contributions from electric and magnetic multipole modes and the interferences between multipole resonances when the Si nanoparticle is placed at P_1 , where the total transverse radiation force and the total contributions from electric and magnetic multipole modes, and the interferences are represented with total, total_{ER} , total_{MR} , and total_{inter} , respectively. It can be seen that the nanoparticles receive a large negative ($-x$ direction) radiation force when the wavelength is longer than $\lambda = 0.683 \mu\text{m}$ and a relatively small positive ($+x$ direction) radiation force with the decrease of the wavelength from $\lambda = 0.683 \mu\text{m}$. The maximum value of the negative radiation force is 1.7 pN at $\lambda = 0.947 \mu\text{m}$, which is three orders of magnitude larger than that of the Brownian force that is about 0.005 pN at room temperature [34]. From the decomposition of the total radiation force, as shown in Eq. (A12), it can be seen that the total transverse radiation

force is dominated not only by the magnetic and electric multipole modes but also the hybridizations between different resonant modes. In order to investigate the contributions from a single mode or single interference, we further decompose the total force from magnetic (electric) resonant modes into the contributions from MD (ED), MQ (EQ), and magnetic octupole MO (electric octupole, EO) respectively, as shown in Figs. 2(b) and 2(c). Similarly, the contributions for the interferences can also be divided into the contributions from the interferences between two magnetic (electric) multipole modes (MM and EE) and magnetic and electric multipole modes (EM), as shown in Fig. 2(d). Close inspections of force spectra of magnetic and electric multipole modes in Figs. 2(b) and 2(c) show that each mode can provide positive and negative contributions with the variation of the wavelength, and it should be pointed out that the largest force contributions do not take place at magnetic or electric resonance wavelengths. Compared with the decomposition of the total scattering spectrum [see Fig. 1(b)], it can be seen that the main negative contributions from the magnetic and electric multipole modes locating at $\lambda = 1.003 \mu\text{m}$ for MD and ED, $\lambda = 0.706 \mu\text{m}$, $\lambda = 0.619 \mu\text{m}$ for MQ and EQ, and $\lambda = 0.572 \mu\text{m}$ for MO, which, respectively, correspond to the dipole, quadrupole, and octupole Kerker conditions, whereas these multipole modes provide the main positive contributions, positioned at $\lambda = 0.870 \mu\text{m}$, $\lambda = 0.670 \mu\text{m}$, and $\lambda = 0.560 \mu\text{m}$ for MD, MQ, and MO, and $\lambda = 0.688 \mu\text{m}$ and $\lambda = 0.576 \mu\text{m}$ for ED and EQ, which, respectively, correspond to the dipole, quadrupole, and octupole anti-Kerker conditions. These dynamics behaviors are totally distinct from the cases that the nanoparticles are put on the propagation of the Gaussian beam [28] and the case that the nanoparticles are excited by the plane wave [35].

Besides the contribution of magnetic and electric multipoles, the interferences among different multipolar modes also provide a prominent contribution to the total transverse radiation force, as shown in Eq. (A12). From Fig. 2(a), it can be clearly seen that the interferences between multipole modes mainly introduce negative contributions to the total transverse radiation force. By further decomposing the total contribution from the interferences into three components from EM, MM, and EE [see Fig. 2(d)], we can see that the contribution from the interferences is mainly dominated by the EM and EE, while the MM only provides a tiny contribution in the short wavelength. These results can be explained by the decomposition of the total scattering spectrum [see Fig. 1(b)] that the same order magnetic and electric multipole modes can support prominent interaction in a wide wavelength range. For the EE, although there is a magnetic multipole resonant mode between the adjacent order electric multipole modes, a certain interaction can also be realized because of their wide resonant spectra. However, due to the narrow resonant spectra width and a large separation between neighboring magnetic multipole modes, no obvious interaction can be achieved.

Now let us consider the case that the nanoparticle is located at P_2 . Similar to the case discussed above, we just consider only the y component of radiation force due to symmetry of the electric field and geometric shape. It can be seen that the total radiation spectrum presented in Fig. 3(a) is totally different from that of the first case even though the total

radiation force is also dominated by magnetic, electric multipole modes, and the interaction between different multipole modes. The nanoparticle also receives alternative negative and positive radiation force with the decrease of wavelength. By comparison with Figs. 2(b) and 2(c), one can see that the decomposed force contributions of the magnetic and electric multipole modes remain the same variation trend as that of the first case, and the largest negative and positive radiation forces exist at the wavelengths fulfilling the Kerker and anti-Kerker conditions, as shown in Figs. 3(b) and 3(c). It is worth noting that the electric multipole modes provide more contribution to the total radiation force than the magnetic ones, which is just reverse of the first case. For the contribution of multipole mode interference [see Fig. 3(d)], the interference-induced radiation force is dominated by the EM and MM, and the EE totally has no contribution to the radiation force. Interestingly, the EM provides the positive contribution, while the MM induces the negative contribution, which results in a totally positive contribution to the total radiation force.

In order to explore the underlying physical insights about the modulations of the radiation forces in Kerker (anti-Kerker) conditions. We calculate the far-field scattering patterns at the wavelengths fulfilling the Kerker and anti-Kerker conditions which are indicated by short dashed lines in Figs. 2(a) and 3(a) when the nanoparticle is, respectively, positioned at P_1 and P_2 . Figure 4 presents the far-field scattering patterns when the nanoparticle is placed at P_1 . It can be seen that the forward scattering can be dramatically improved and the backward scattering is totally suppressed by the destructive interference between the MD and ED for the dipolar Kerker condition ($\lambda = 1.003 \mu\text{m}$) [36–38], as shown in Fig. 4(a). On the contrary, for the dipolar anti-Kerker condition ($\lambda = 0.870 \mu\text{m}$) shown in Fig. 4(b) one can see that the forward scattering can be partly suppressed, leading to an enhanced backward scattering. From Figs. 2(a) and 2(b), it can be seen that the high-order Kerker condition, such as the quadrupolar Kerker condition, cannot be achieved due to the off-resonance contribution of ED and MD, but another multipolar Kerker and anti-Kerker conditions, which originate from the constructive and destructive interferences of dipoles (ED and MD) and quadrupoles (EQ and MQ) can be partly fulfilled [39,40]. For the case considered in this work, the multipolar Kerker and anti-Kerker conditions take place at $\lambda = 0.706 \mu\text{m}$ and $\lambda = 0.53 \mu\text{m}$. The far-field radiation patterns which correspond to the dipolar-quadrupolar Kerker and anti-Kerker conditions are shown in Figs. 4(c) and 4(d). For $\lambda = 1.003 \mu\text{m}$ there are four radiation lobes corresponding to the forward, backward, and side scattering, where the sidelobes oriented along the H polarization direction (y axis) are leading by MQ [41], as shown in Fig. 4(c). For the multipolar anti-Kerker condition, however, the backward scattering is completely suppressed due to the destructive interference between the dipoles and quadrupoles. An interesting feature shown in Fig. 4 is that the total far-field scattering patterns in the E - K plane demonstrate asymmetric distributions referring to the beam propagation direction (K direction) due to the asymmetry of the electric field when the nanoparticle is placed at P_1 , which provides scattering component pointing to the x direction. But, for the H plane, it can be seen that the far-field scattering shows completely symmetric distribution at all considered wavelengths, which

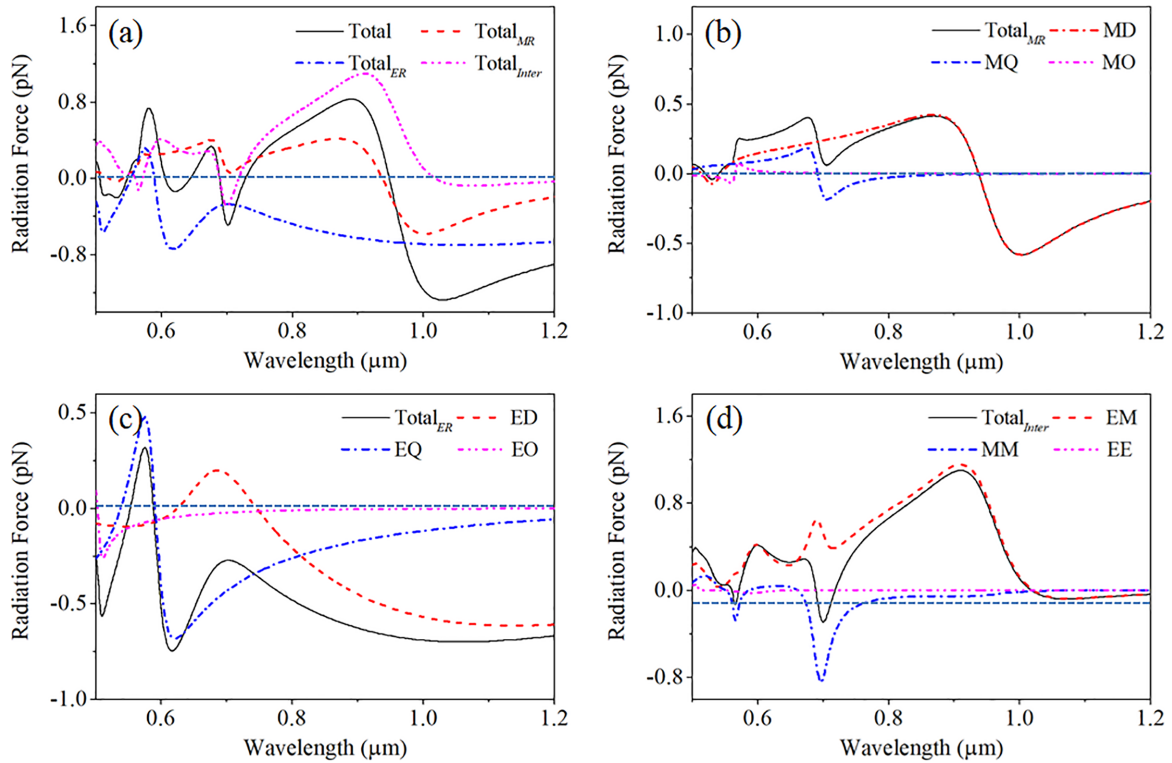


FIG. 3. The total transverse radiation force and the corresponding decomposition when the Si nanoparticle is placed at P_2 . (a) The total transverse radiation force (total) and the contributions from the magnetic ($total_{MR}$) and electric ($total_{ER}$) multipoles and interferences of both modes ($total_{inter}$). (b) The contribution from the magnetic multipoles and the corresponding decomposition (MD, MQ, and MO). (c) The contribution from the electric multipoles and the corresponding decomposition (ED, EQ, and EO). (d) The contribution from the interference of both kinds of modes and the corresponding decomposition (EM, MM, and EE).

causes no net momentum in the y direction. Hence, there is no transverse radiation force acting on the nanoparticle in the y direction. As a result, the total radiation moment along with the x positive or negative directions depends on not only the side scattering but also the forward and backward

scatterings, which in turn dominates the directions of the transverse radiation forces exerted on the nanoparticle. For the dipole Kerker condition, one can see from Fig. 4(a) that the total scattering component in x directions along with the positive direction, which leads to a negative radiation force

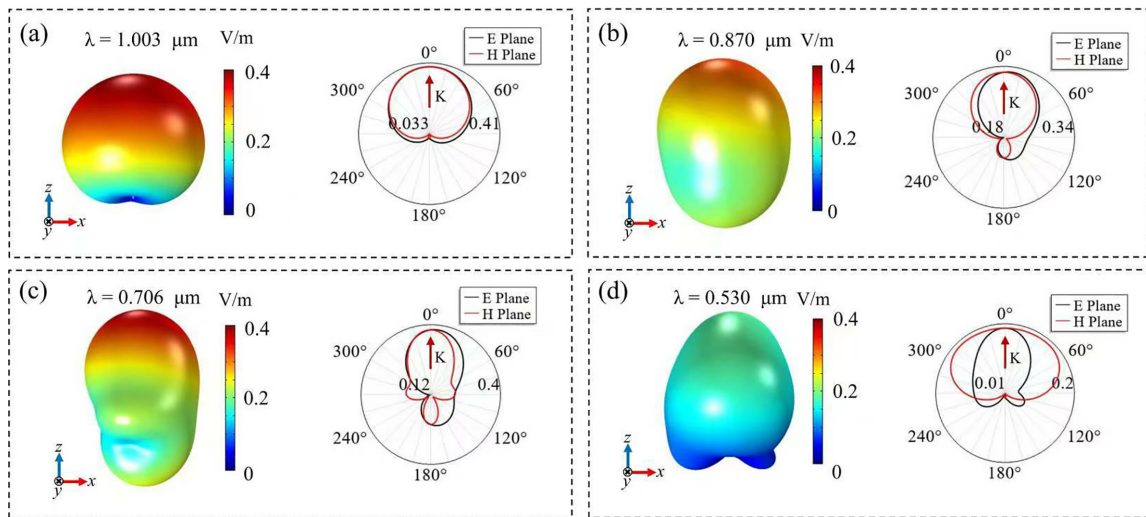


FIG. 4. The three-dimensional (3D) and two-dimensional (2D) far-field scattering patterns for the silicon nanoparticle positioned in P_1 at the four typical wavelengths: (a) $\lambda = 1.003 \mu\text{m}$, (b) $\lambda = 0.870 \mu\text{m}$, (c) $\lambda = 0.706 \mu\text{m}$, and (d) $\lambda = 0.530 \mu\text{m}$. The far-field scattering pattern in E plane and H plane indicated by black and red lines.

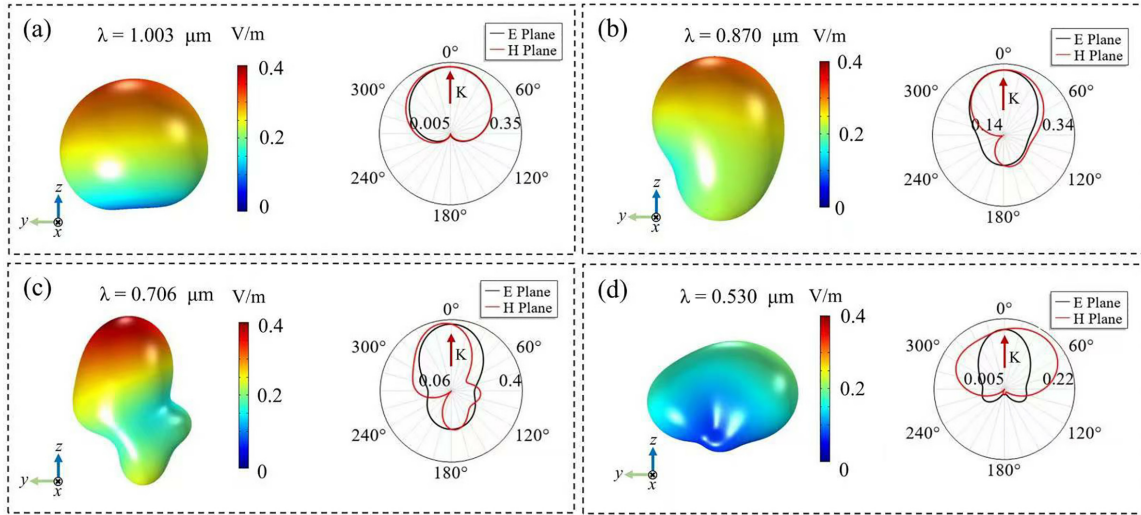


FIG. 5. The 3D and 2D far-field scattering patterns for the silicon nanoparticle positioned in P_2 at the four typical wavelengths: (a) $\lambda = 1.003 \mu\text{m}$, (b) $\lambda = 0.870 \mu\text{m}$, (c) $\lambda = 0.706 \mu\text{m}$, and (d) $\lambda = 0.530 \mu\text{m}$. The far-field scattering pattern in E plane and H plane indicated by black and red lines.

acting on the nanoparticle, as shown in Fig. 2(a). For the dipole anti-Kerker condition, one can see that for the total radiation moment in the x direction remains pointing to the x positive direction though the backward scattering is enhanced in some degree, as depicted in Fig. 4(b). Therefore, the nanoparticle still receives the negative radiation force, as shown in Fig. 2(a). Similar to the dipole Kerker condition, for the case of dipole-quadrupole Kerker condition ($\lambda = 0.706 \mu\text{m}$) one can see from Fig. 4(c) that the transverse scattering is mainly controlled by the ED; the transverse scattering collimates in the x positive direction, which also introduces a negative transverse pulling radiation force on the nanoparticle. It should be mentioned that owing to the light intensity inhomogeneity in the focus plane of the Gaussian beam, the total radiation force calculated in this paper also can be decomposed of the gradient force and the scattering force [28]. For the above three cases shown in Figs. 4(a)–4(c), the negative scattering force and the gradient force collectively enhance the pulling action on the nanoparticle, and result in a negative radiation force [Fig. 2(a)]. For multipole anti-Kerker condition ($\lambda = 0.530 \mu\text{m}$), it can be seen from Fig. 4(d) that the radiation moment in the x direction mainly focuses in the x negative direction, which means that the nanoparticle receives a repulsive scattering force and this force is large enough to balance the gradient force. As a consequence, the nanoparticle receives almost no transverse radiation force, as presented in Fig. 2(a), while in the H plane it can be seen that the far-field scatterings, either the MD or MQ, at all considered wavelengths show completely symmetric distribution which causes no net momentum in the y direction. As a result, there is no y -component radiation force acting on the nanoparticles.

Figure 5 presents the far-field scattering patterns at Kerker and anti-Kerker conditions when the silicon nanoparticle is positioned on P_2 . One can clearly see that the far-field scattering patterns at corresponding wavelengths remain unchanged, while the asymmetry of the far-field radiation referring to the K direction, which determines the total transverse radiation force, is transferred from the E plane to the H plane. For

the case of dipole Kerker condition ($\lambda = 1.003 \mu\text{m}$), one can see from Fig. 5(a) that the forward scattering direction deviates from the K direction to the positive direction of the y axis due to the asymmetry of the magnetic field, which in turn introduces a negative transverse radiation force acting on the silicon nanoparticle, as shown in Fig. 3(a). However, for the anti-Kerker condition ($\lambda = 0.870 \mu\text{m}$), the scattering component in the $-y$ direction is greater than that in the $+y$ direction, resulting a large scattering force along with the $+y$ direction. Therefore, it can be seen from Fig. 3(a) that a positive radiation force exerted on the nanoparticle, although there is a gradient force acting on the nanoparticle. For the multipolar dipole-quadrupole Kerker and anti-Kerker conditions, one can see from Figs. 5(c) and 5(d) that the scattering component along with the y direction is not only dominated by the dipole mode, and the quadrupole mode also plays an important role in tailoring the optical radiation force on the nanoparticle, which is totally different from the case that the nanoparticle is positioned in P_1 . As for the dipole-quadrupole Kerker condition, it can be seen from Fig. 5(c) that the transverse y -scattering component includes two parts: one is from the forward scattering and backward scattering in the z direction, and the other comes from the side scattering along with the y direction. Obviously, the scattering intensity pointing to the y -positive direction is much larger than that in the inverse direction, which results in a negative transverse radiation force acting on the nanoparticle, as shown in Fig. 3(a). From the case of the multipole anti-Kerker condition, it can be seen from Fig. 5(d) that the side scattering almost dominates transverse scattering with the suppression of the backward scattering; the scattering component in the $-y$ direction is slightly larger than that in the $+y$ direction, resulting in a positive scattering force acting on the nanoparticles. Obviously, the scattering force is not large enough to balance the gradient force. Therefore, we can see from Fig. 3(a) that the nanoparticle receives a negative transverse radiation force.

All these results discussed above manifest that a tunable radiation force acting on the Si nanoparticle can be induced

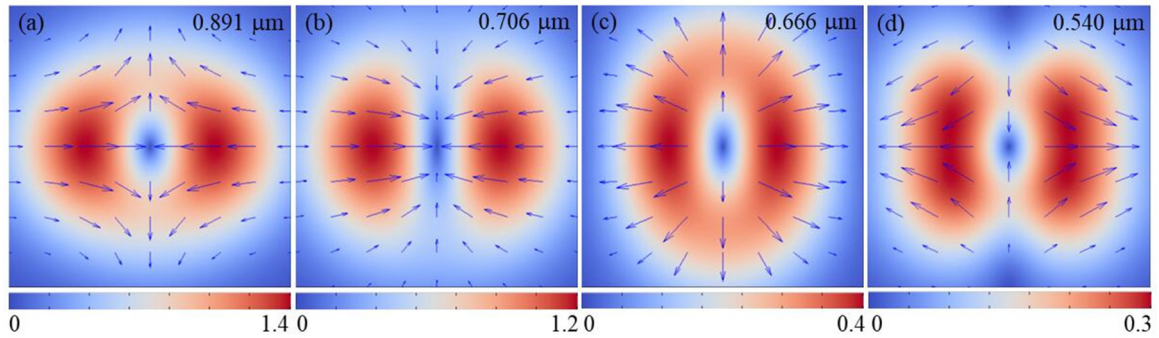


FIG. 6. The distribution of the total transverse radiation force, F_{total} of the focus plane at $0.891 \mu\text{m}$ (a), $0.706 \mu\text{m}$ (b), $0.666 \mu\text{m}$ (c), and $0.540 \mu\text{m}$ (d), respectively. The arrows in figures represent the direction of the force, and the length (the color) represents the relative magnitude of the force. The unit of force (color bar) is pN.

by the hybridization of electric and magnetic modes, which also means that the Si nanoparticle can show totally different dynamic behaviors when it is excited by tightly focused laser beams with different wavelengths. In order to further confirm this conclusion, we calculate the distribution of the total transverse radiation force in the focus plane at four typical wavelengths (0.891 , 0.706 , 0.666 , and $0.540 \mu\text{m}$) which are shown in Fig. 6. As for $\lambda = 0.891 \mu\text{m}$, it can be seen from Fig. 6(a) that the nanoparticle can receive a pulling force in the x direction, while it receives a pushing force in the y direction. On the contrary, as for $\lambda = 0.540 \mu\text{m}$, the nanoparticle can obtain a pushing force in the x direction and a pulling force in the y direction, as shown in Fig. 6(d). For the other two cases, the nanoparticle will receive the same type of radiation force either in the x direction or in the y direction. For the case of $\lambda = 0.706 \mu\text{m}$, one can see from Fig. 6(b) that the nanoparticle receives a total pulling force that can be applied to strength of the transverse trapping efficiency of the optical tweezers. But, for $\lambda = 0.666 \mu\text{m}$, it can be seen that a total pushing force acts on the nanoparticle which can find potential application in sieving of nanoparticle.

It is well known that the higher-order Mie resonances can be excited as the size of the nanoparticle increases, which means that the hybridizations among different multipoles and the induced transverse scattering forces acting on the nanoparticle can be enriched. In the view of practical trapping of nanoparticles, the laser wavelength and the trapping efficiency are the most considered factors. Thus, it is very important to examine the evolution of the transverse radiation force with the increase of the size of the nanoparticle. Based on the analysis above, we calculate the evolutions of the total transverse radiation forces, the total contribution from electric and magnetic modes corresponding to the Kerker and anti-Kerker conditions, and the contribution from the interferences between electric and magnetic modes as a function of the size of the nanoparticle and the wavelength when the nanoparticle is positioned in P_1 and P_2 . The results are presented in Fig. 7. It can be seen that there exist more bands where the nanoparticle can receive transverse pulling or pushing force when more high-order multipoles are excited effectively with the increase of the particle size in the considered wavelength range (0.4 – $1.8 \mu\text{m}$), as shown in the left column of Fig. 7. By comparing the contributions to the total radiation force from the electric and magnetic resonances (shown in the

middle column of Fig. 7), the nanoparticles with different sizes mainly receive the transverse pushing force in the considered wavelength range (except for the dipole Kerker point) in the x direction, while in the y direction, the transverse pulling force dominates the dynamics of the nanoparticles in almost all wavelengths and there is only a narrow band where the nanoparticles receive the transverse pushing force. But, for the contribution from the hybridization of electric and magnetic multipoles, only transverse pulling force (pushing force) acts on the nanoparticles in x direction (y direction), as shown in the right column of Fig. 7. In addition, it can be seen that the maxima of transverse radiation forces (pulling and pushing forces) shift to the long-wavelength side with the increase of the size, resulting that Si nanoparticles with different size can receive totally different radiation force, which can be used to direction guide transportation, selected optical trapping, and sieving of nanoparticles.

III. CONCLUSION

We investigate theoretically the transverse radiation force acting on the Si nanoparticles with the illumination of a linearly polarized Gaussian by using the MST method combined with GLMT. It is demonstrated that the radiation force can be tuned flexibly by electric–magnetic multipolar resonances and the hybridization of the both kinds of resonances. By decomposing the radiation force into three components from the electric multipolar resonances, magnetic multipolar resonances, and the interference among different resonances, it can be found that the nanoparticle can receive the transverse pulling force and pushing force due to the Kerker and the anti-Kerker effects. In order to explore the insight about the modulations of radiation force by the Kerker and anti-Kerker effects, we calculate the far-field radiation patterns at these wavelengths fulfilling the Kerker and anti-Kerker conditions. The results show that transverse pulling and the pushing forces mainly originate from the asymmetric distribution of the far-field radiation pattern. The results presented in this work can shed light on the dynamics interaction between nanoparticles with high refractive index and the tightly focused laser beam. Other applications, such as the enhancement of the optical pulling force or pushing force in the optical trapping, can also be realized by using Si nanoparticles.

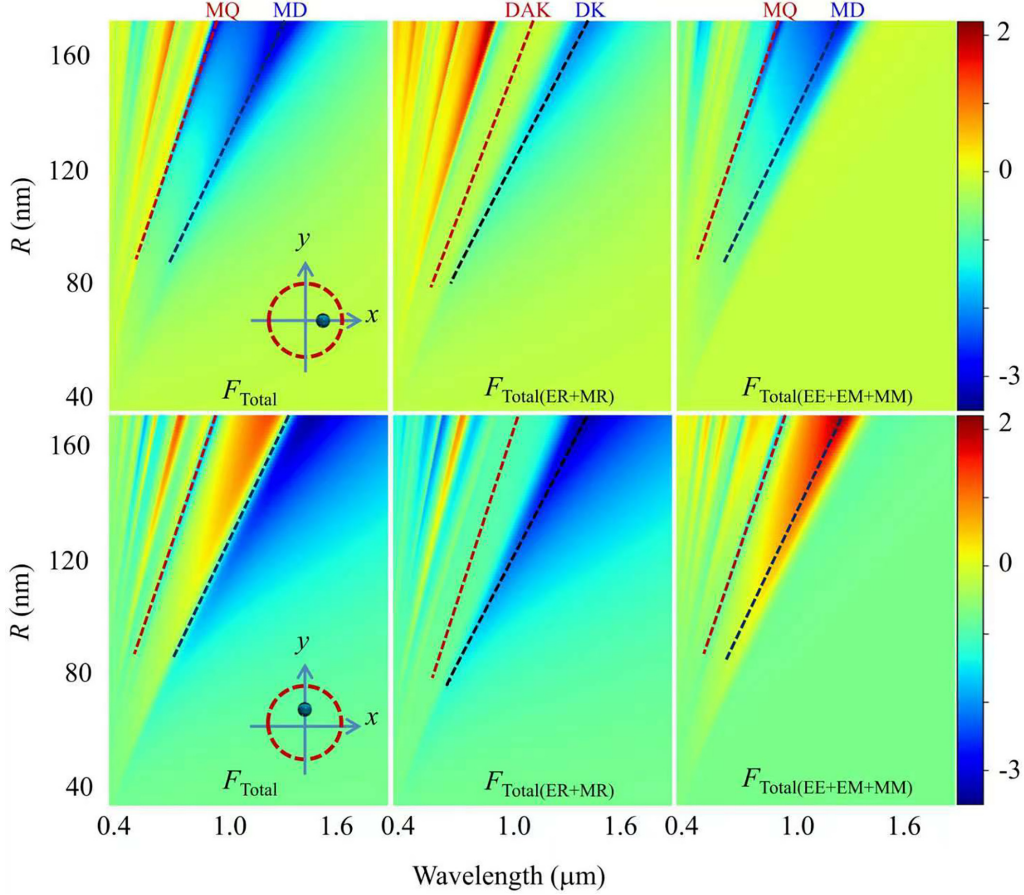


FIG. 7. Total transverse force F_{Total} (the first column), the contribution from the electric resonances (ER) and magnetic resonances (MR) $F_{\text{Total(ER+MR)}}$ (the second column), and the contribution from the hybridization of electric and magnetic multipoles (EE, EM, and MM) $F_{\text{Total(EE+EM+MM)}}$ (the third column) as a function of the wavelength and the radii of the nanoparticle when the nanoparticle is placed at P_1 (the upper panel) and P_2 (the lower panel), respectively. The color in this figure represents the magnitude of the force with a unit of pN.

ACKNOWLEDGMENTS

The authors are grateful to the Key-Area Research and Development Program of Guangdong Province (Grant No. 2019B020219002), the National Natural Science Foundation of China (Grants No. 12174120 and No. 11774099), the Guangdong Basic and Applied Basic Research Foundation (Grants No. 2022A1515010411 and No. 2021A1515012112), and the Laboratory of Lingnan Modern Agriculture project (Grant No. NT2021009) for the support to the work.

APPENDIX

1. Scattering cross section and optical radiation forces calculation

We define the original beam-coordinate system O_{xyz} so that the center of the Gaussian beam waist is located at point O , and the particle is illuminated by an x polarized at the waist Gaussian beam propagating in the z -axis direction. The

center of the particle is located at the point O' of a Cartesian coordinate system $O'x'y'z'$, and the Cartesian coordinates of O' in the system O_{xyz} are (x_0, y_0, z_0) . And, we can expand the electromagnetic component of the incident Gaussian beam (designated by the superscript i) using spherical vector wave functions (SVWFs) as follows [42]:

$$\mathbf{E}^i = E_0 \sum_{n=1}^{\infty} \sum_{m=-n}^n C_{nm} [b_{mn}^i \mathbf{M}_{nm}^{(1)}(kr, \theta, \varphi) + a_{mn}^i \mathbf{N}_{nm}^{(1)}(kr, \theta, \varphi)], \quad (\text{A1})$$

where E_0 is the electric field strength, θ and φ are the polar and azimuthal angles of the spherical coordinate system, respectively; the wave number is denoted by $k = 2\pi/\lambda$, and C_{nm} are normalization factors, which can be obtained by

$$C_{nm} = \begin{cases} i^{n-1} \frac{2n+1}{n(n+1)}, & m \geq 0 \\ (-1)^{|m|} \frac{(n+|m|)!}{(n-|m|)!} i^{n-1} \frac{2n+1}{n(n+1)}, & m < 0 \end{cases}, \quad (\text{A2})$$

and $M_{nm}^{(l)}$ and $N_{nm}^{(l)}$ are the SVWFs, which are calculated as [43]

$$\begin{aligned} M_{nm}^{(l)}(kr, \theta, \varphi) = z_n^{(l)}(kr) \left[im \frac{P_n^m(\cos \theta)}{\sin \theta} \hat{\theta} - \frac{dP_n^m(\cos \theta)}{d\theta} \hat{\varphi} \right] e^{im\varphi} N_{nm}^{(l)}(kr, \theta, \varphi) = n(n+1) \frac{z_n^{(l)}(kr)}{kr} P_n^m(\cos \theta) e^{im\varphi} \hat{r} \\ + \frac{1}{kr} \frac{d(rz_n^{(l)}(kr))}{dr} \left[im \frac{P_n^m(\cos \theta)}{\sin \theta} \hat{\varphi} + \frac{dP_n^m(\cos \theta)}{d\theta} \hat{\theta} \right] e^{im\varphi}, \end{aligned} \quad (A3)$$

in which $z_n^{(l)}(x)$ represents an appropriate kind of spherical Bessel functions: the first kind j_n , or the third kind $h_n^{(1)}$ denoted by $l = 1$, or 3, respectively; $P_n^m(\cos \theta)$ is the associated Legendre function of the first kind.

And, a_{mn}^i and b_{mn}^i are called beam-shaped coefficients, which are obtained through the localized approximations with sum of series given by Doicu [42]; the detailed description on the localized approximation can be found in Refs. [44,45].

$$\begin{bmatrix} a_{mn}^i \\ b_{mn}^i \end{bmatrix} = (-1)^{m-1} K_{nm} \psi_0^0 e^{ikz_0} \frac{1}{2} \left[e^{i(m-1)\varphi} J_{m-1} \left(2 \frac{\bar{Q} \rho_0 \rho_n}{w_0^2} \right) \pm e^{i(m+1)\varphi} J_{m+1} \left(2 \frac{\bar{Q} \rho_0 \rho_n}{w_0^2} \right) \right], \quad (A4)$$

where

$$\begin{aligned} \psi_0^0 = i\bar{Q} \exp(-i\bar{Q}\rho_0^2/w_0^2) \exp[-i\bar{Q}(n+0.5)^2/(k^2w_0^2)], \\ K_{nm} = \begin{cases} \frac{n(n+1)}{n+0.5}, & m = 0 \\ (-i)^{|m|} \frac{i}{(n+0.5)^{|m|-1}}, & m \neq 0 \end{cases}, \quad \rho_n = \frac{n+0.5}{k}, \quad \rho_0 = \sqrt{x_0^2 + y_0^2}, \quad \bar{Q} = \left(i - \frac{2z_0}{kw_0^2} \right)^{-1}, \quad \varphi = \arctan \frac{x_0}{y_0}. \end{aligned} \quad (A5)$$

The electromagnetic component of the scattered field (designated by the superscript s) can be expanded in terms of the SVWFs as [43]

$$\mathbf{E}^s = E_0 \sum_{n=1}^{\infty} \sum_{m=-n}^n [A_{nm}^s \mathbf{M}_{nm}^{(3)}(kr, \theta, \varphi) + B_{nm}^s \mathbf{N}_{nm}^{(3)}(kr, \theta, \varphi)], \quad (A6)$$

where A_{nm}^s and B_{nm}^s are called Gaussian beam-scattering coefficients, and for uniaxial isotropic spherical particles, they can be derived in the textbook of Ref. [46]:

$$A_{nm}^s = C_{nm} a_{mn}^i a_n, \quad B_{nm}^s = C_{nm} b_{mn}^i b_n, \quad (A7)$$

in which a_n and b_n are the scattering coefficients of plane wave; if we take the permeability of the particle and the surrounding medium to be the same, then [47]

$$\begin{aligned} a_n = \frac{m\psi_n(mx)\psi_n'(x) - \psi_n(x)\psi_n'(mx)}{m\psi_n(mx)\xi_n'(x) - \xi_n(x)\psi_n'(mx)}, \\ b_n = \frac{\psi_n(mx)\psi_n'(x) - m\psi_n(x)\psi_n'(mx)}{\psi_n(mx)\xi_n'(x) - m\xi_n(x)\psi_n'(mx)}, \end{aligned} \quad (A8)$$

where the size parameter $x = 2\pi N_m a / \lambda$, and a is particle radius, λ is wavelength of incident light; the relative refractive index $m = N_p / N_m$ and N_p and N_m are the refractive indices of particle and medium, respectively; $\psi_n(x)$ and $\xi_n(x)$ are Riccati-Bessel functions.

We can obtain the Gaussian beam-scattering cross section C_{sca} by the expression [46]

$$C_{\text{sca}} = \frac{\lambda^2}{\pi N_m^2} \sum_{n=1}^{\infty} \sum_{m=-n}^n \frac{2n+1}{n(n+1)} \frac{(n+|m|)!}{(n-|m|)!} \{|a_n|^2 |a_{mn}^i|^2 + |b_n|^2 |b_{mn}^i|^2\}. \quad (A9)$$

When a strongly convergent laser beam illuminates a particle, part of the momentum will be transferred from the laser beam to the particle due to the process of scattering. The time-averaged optical radiation force $\langle F \rangle$ can be computed by the integration of the Maxwell stress tensor T over the surface S enclosing the particle [48],

$$\langle F \rangle = \oint_S \langle \mathbf{T} \cdot \hat{r} \rangle dS, \quad (A10)$$

where tensor $\mathbf{T} = \varepsilon \mathbf{E} \mathbf{E} + \mu \mathbf{H} \mathbf{H} - 1/2(\varepsilon E^2 + \mu H^2) \delta$, and δ is a unit matrix; \hat{r} is the normal unit vector pointing out from the surface; and ε and μ denote the permittivity and permeability of the surrounding medium, respectively. The electromagnetic field includes the incident and scattered field $\mathbf{E} = \mathbf{E}^i + \mathbf{E}^s$, $\mathbf{H} = \mathbf{H}^i + \mathbf{H}^s$. Moreover, in spherical coordinate system, formula (A10) can be written as

$$\langle F \rangle = \oint_S \left\langle \varepsilon E_r \mathbf{E} + \mu H_r \mathbf{H} - \frac{1}{2}(\varepsilon E^2 + \mu H^2) \hat{r} \right\rangle dS. \quad (A11)$$

Using the relations between coordinates of Cartesian coordinate system and sphere coordinate system, substituting the expressions of the incident and scattered field and then utilizing the orthogonality of associated Legendre functions and trigonometric functions and the approximate expressions of Riccati-Bessel functions at $r \gg \lambda$, we can obtain the analytical expressions of the transverse radiation forces F_x and F_y and axial radiation force F_z as follows [49]

$$\begin{aligned}
F_x + iF_y = & \frac{N_m P}{\pi c k_0^2 w_0^2} \sum_{n=1}^{\infty} \sum_{m=-n}^n [\sqrt{(n-m)(n+m+1)} N_{nm}^{-1} N_{n+1}^{-1} (a_{nm}^i B_{nm+1}^{s*} + b_{nm}^j A_{nm+1}^{s*}) \\
& + B_{nm}^s a_{nm+1}^{i*} + A_{nm}^s b_{nm+1}^{j*} + 2A_{nm}^s B_{nm+1}^{s*} + 2B_{nm}^s A_{nm+1}^{s*}) \\
& - i \sqrt{\frac{(n-m-1)(n-m)}{(2n-1)(2n+1)}} (n-1)(n+1) N_{nm}^{-1} N_{n-1}^{-1} (a_{nm}^i A_{n-1m+1}^{s*} + b_{nm}^j B_{n-1m+1}^{s*} \\
& + A_{nm}^s a_{n-1m+1}^{i*} + B_{nm}^s b_{n-1m+1}^{j*} + 2A_{nm}^s A_{n-1m+1}^{s*} + 2B_{nm}^s B_{n-1m+1}^{s*}) \\
& - i \sqrt{\frac{(n+m+1)(n+m+2)}{(2n+1)(2n+3)}} n(n+2) N_{nm}^{-1} N_{n+1}^{-1} (a_{nm}^i A_{n+1m+1}^{s*} + b_{nm}^j B_{n+1m+1}^{s*} \\
& + A_{nm}^s a_{n+1m+1}^{i*} + B_{nm}^s b_{n+1m+1}^{j*} + 2A_{nm}^s A_{n+1m+1}^{s*} + 2B_{nm}^s B_{n+1m+1}^{s*})], \tag{A12}
\end{aligned}$$

$$\begin{aligned}
F_z = & \frac{2N_m P}{\pi c k_0^2 w_0^2} \text{Re} \sum_{n=1}^{\infty} \sum_{m=-n}^n \left[in(n+2) \sqrt{\frac{(n-m+1)(n+m+1)}{(2n+1)(2n+3)}} N_{nm}^{-1} N_{n+1}^{-1} (a_{n+1m}^i A_{nm}^{s*} \right. \\
& + b_{n+1m}^j B_{nm}^{s*} + A_{n+1m}^s a_{nm}^{i*} + B_{n+1m}^s b_{nm}^{j*} + 2A_{n+1m}^s A_{nm}^{s*} + 2B_{n+1m}^s B_{nm}^{s*}) \\
& \left. - m N_{nm}^{-2} (a_{nm}^i B_{nm}^{s*} + b_{nm}^j A_{nm}^{s*} + 2A_{nm}^s B_{nm}^{s*}) \right]. \tag{A13}
\end{aligned}$$

where the superscript sign “*” represents the conjugate of the variable, c is the speed of light in vacuum, P denotes the power of the incident Gaussian beam, and

$$N_{nm} = \sqrt{(2n+1)(n-m)!/[4\pi(n+m)!]}, \quad (m = 0, \pm 1, \dots, \pm n). \tag{A14}$$

2. Far-field radiation pattern based on the GLMT

Based on the GLMT [46], the far-field radiation pattern can be calculated with the following equation:

$$\frac{I_{\theta}^+}{I_{\varphi}^+} = \frac{\lambda^2}{4\pi^2 r^2} \left| \frac{S_2}{S_1} \right|^2 \tag{A15}$$

where S_1 and S_2 can be calculated with the following expressions

$$\begin{aligned}
S_1 = & \sum_{n=1}^{\infty} \sum_{m=-n}^n \frac{2n+1}{n(n+1)} \left[mA_{nm}^s b_{nm}^j \frac{P_n^m(\cos \theta)}{\sin \theta} + iB_{nm}^s a_{nm}^i \frac{dP_n^m(\cos \theta)}{d\theta} \right] \exp(im\varphi) \\
S_2 = & \sum_{n=1}^{\infty} \sum_{m=-n}^n \frac{2n+1}{n(n+1)} \left[A_{nm}^s b_{nm}^j \frac{dP_n^m(\cos \theta)}{d\theta} + imB_{nm}^s a_{nm}^i \frac{P_n^m(\cos \theta)}{\sin \theta} \right] \exp(im\varphi)
\end{aligned}$$

- [1] S. Q. Dai, J. Y. Mi, J. Z. Dou, H. Lu, C. Dong, L. Ren, R. Zhao, W. P. Shi, N. Zhang, Y. D. Zhou, J. W. Zhang, J. L. Di, and J. L. Zhao, Optical tweezers integrated surface plasmon resonance holographic microscopy for characterizing cell-substrate interactions under noninvasive optical force stimuli, *Biosens. Bioelectron.* **206**, 114131 (2022).
- [2] Y. Morino and S. Kanada, Degradation analysis by X-ray absorption spectroscopy for LiNbO₃ coating of sulfide-based

all-solid-state battery cathode, *ACS Appl. Mater. Interfaces.* **15**, 2979 (2023).

- [3] C.-Y. Li, T. Zhang, Y.-F. Kang, C.-B. Qi, B. Zheng, C.-M. Xu, Y. Lin, D.-W. Pang, and H.-W. Tang, Incorporating luminescence-concentrating upconversion nanoparticles and DNA walkers into optical tweezers assisted imaging: A highly stable and ultrasensitive bead supported assay, *Chem. Commun.* **56**, 6997 (2020).

- [4] N. B. Vilas, C. Hallas, L. Anderegg, P. Robichaud, A. Winnicki, D. Mitra, and J. M. Doyle, Magneto-optical trapping and sub-Doppler cooling of a polyatomic molecule, *Nature (London)* **606**, 70 (2022).
- [5] W. C. Wang, Y. Tao, J. C. Fan, Z. P. Yan, H. Shang, D. L. Phillips, M. Chen, and G. S. Li, Fullerene-graphene acceptor drives ultrafast carrier dynamics for sustainable CdS photocatalytic hydrogen evolution, *Adv. Funct. Mater.* **32**, 2201357 (2022).
- [6] J. T. Wilson, S. Saskin, Y. Meng, S. Ma, R. Dilip, A. P. Burgers, and J. D. Thompson, Trapping alkaline earth Rydberg atoms optical tweezer arrays, *Phys. Rev. Lett.* **128**, 033201 (2022).
- [7] D. Bluvstein, H. Levine, G. Semeghini, T. T. Wang, S. Ebadi, M. Kalinowski, A. Keesling, N. Maskara, H. Pichler, M. Greiner, V. Vuletić, and M. D. Lukin, A quantum processor based on coherent transport of entangled atom arrays, *Nature (London)* **604**, 451 (2022).
- [8] S. Ma, A. P. Burgers, G. Y. Liu, J. Wilson, B. C. Zhang, and D. J. Thompson, Universal gate operations on nuclear spin qubits in an optical tweezer array of Yb-171 atoms, *Phys. Rev. X* **12**, 021028 (2022).
- [9] A. Ashkin, Acceleration and trapping of particles by radiation pressure, *Phys. Rev. Lett.* **24**, 156 (1970).
- [10] Y. Z. Shi, S. Xiong, L. K. Chin, J. B. Zhang, W. Ser, J. H. Wu, T. N. Chen, Z. C. Yang, Y. L. Hao, B. Liedberg, P. H. Yap, D. P. Tsai, C.-W. Qiu, and A. Q. Liu, Nanometer-precision linear sorting with synchronized optofluidic dual barriers, *Sci. Adv.* **4**, 1 (2018).
- [11] G. Spektor, D. Kilbane, A. K. Mahro, B. Frank, S. Ristok, L. Gal, P. Kahl, D. Podbiel, S. Mathias, H. Giessen, F.-J. Meyer zu Heringdorf, M. Orenstein, and M. Aeschlimann, Revealing the subfemtosecond dynamics of orbital angular momentum in nanoplasmonic vortices, *Science* **355**, 1187 (2017).
- [12] R. C. Jin, J. Q. Li, L. Lin, Z. G. Dong, and Y. M. Liu, Dual-mode subwavelength trapping by plasmonic tweezers based on V-type nanoantennas, *Opt. Lett.* **44**, 319 (2019).
- [13] R. R. Agayan, F. Gittes, R. Kopelman, and C. F. Schmidt, Optical trapping near resonance absorption, *Appl. Opt.* **41**, 2318 (2002).
- [14] W. H. Huang, S. F. Li, H. T. Xu, Z. X. Xiang, Y. B. Long, and H. D. Deng, Tunable optical forces enhanced by plasmonic mode hybridization in optical trapping of gold nanorods with plasmonic nanocavity, *Opt. Express* **26**, 6202 (2018).
- [15] K. C. Toussaint, M. Liu, M. Pelton, M. J. Guffey, P. Guyot-Sionnest, and N. F. Scherer, Plasmon resonance-based optical trapping of single and multiple Au nanoparticles, *Opt. Express* **15**, 12017 (2007).
- [16] N. Wang, W. L. Lu, J. Ng, and Z. F. Lin, Optimized optical “tractor beam” for core-shell nanoparticles, *Opt. Lett.* **39**, 2399 (2014).
- [17] M. Pelton, M. Z. Liu, H. Y. Kim, G. Smith, P. Guyot-Sionnest, and N. F. Scherer, Optical trapping and alignment of single gold nanorods using plasmon resonances, *Opt. Lett.* **31**, 2075 (2006).
- [18] C. Selhuber-Unkel, I. Zins, O. Schubert, C. Sönnichsen, and L. B. Oddershede, Quantitative optical trapping of single gold nanorods, *Nano Lett.* **8**, 2998 (2008).
- [19] J. H. Kang, K. Kim, H. S. Ee, Y. H. Lee, T. Y. Yoon, M. K. Seo, and H. G. Park, Low-power nano-optical vortex trapping via plasmonic diabolito nanoantennas, *Nat. Commun.* **2**, 582 (2011).
- [20] Z. P. Li, M. Käll, and H. X. Xu, Optical forces on interacting plasmonic nanoparticles in a focused Gaussian beam, *Phys. Rev. B* **77**, 085412 (2008).
- [21] A. I. Kuznetsov, A. E. Miroshnichenko, M. L. Brongersma, Y. S. Kivshar, and B. Lukyanichuk, Optically resonant dielectric nanostructures, *Science* **354**, 6314 (2016).
- [22] S. Jahani and Z. Jacob, All-dielectric metamaterials, *Nat. Nanotechnol.* **11**, 23 (2016).
- [23] I. Staude and J. Schilling, Metamaterial-inspired silicon nanophotonics, *Nat. Photonics* **11**, 274 (2017).
- [24] A. D. McFarland and R. P. Van Duyne, Single silver nanoparticles as real-time optical sensors with zeptomole sensitivity, *Nano Lett.* **3**, 1057 (2003).
- [25] H. W. Mu, W. J. Xu, J. W. Lv, C. H. Xu, F. M. Wang, Q. Liu, C. Liu, T. Sun, and P. k. Chu, Dual-band directional scattering with all-dielectric trimer in the near-infrared region, *Appl. Opt.* **58**, 5082 (2019).
- [26] K. P. Devi, P. Goswami, and H. Chaturvedi, Optimization of metal nanoparticles dimensions for efficient energy harvesting device using localized surface plasmon resonance, *Proc. SPIE* **11904**, 119040U (2021).
- [27] V. Valuckas, R. Paniagua-Domínguez, A. Maimaiti, P. P. Patra, S. K. Wong, R. Verre, M. Käll, and A. I. Kuznetsov, Fabrication of monodisperse colloids of resonant spherical silicon nanoparticles: Applications in optical trapping and printing, *ACS Photonics* **6**, 2141 (2019).
- [28] N. O. Länk, P. Johansson, and M. Käll, Directional scattering and multipolar contributions to optical forces on silicon nanoparticles in focused laser beams, *Opt. Express* **26**, 29074 (2018).
- [29] G. Gouesbet, J. A. Lock, and G. Gréhan, Partial-wave representations of laser beams for use in light-scattering calculations, *Appl. Opt.* **34**, 2133 (1995).
- [30] D. J. Griffiths, *Introduction to Electrodynamics* (Benjamin, Montvale, 2008), pp. 362–364.
- [31] J. D. Jackson, *Classical Electrodynamics* (Wiley, Hoboken, 1999), p. 68.
- [32] L. D. Landau and E. M. Lifszyc, *The Classical Theory of Fields* (Pergamon Press, New York, 1975).
- [33] E. D. Palik, *Handbook of Optical Constants of Solids* (Academic Press, New York, 1998), Vol. 3.
- [34] K. Okamoto and S. Kawata, Radiation force exerted on sub-wavelength particles near a nanoaperture, *Phys. Rev. Lett.* **83**, 4534 (1999).
- [35] E. Lee and T. Luo, Negative optical force field on supercavitating titanium nitride nanoparticles by a single plane wave, *Nanophotonics* **11**, 79 (2022).
- [36] Y. H. Fu, A. I. Kuznetsov, A. E. Miroshnichenko, Y. F. Yu, and B. Luk’yanichuk, Directional visible light scattering by silicon nanoparticles, *Nat. Commun.* **4**, 1527 (2013).
- [37] M. Nieto-Vesperinas, R. Gomez-Medina, and J. J. Saenz, Angle-suppressed scattering and optical forces on submicrometer dielectric particles, *Opt. Soc. Am. A* **28**, 54 (2011).
- [38] M. Kerker, D. S. Wang, and C. L. Giles, Electromagnetic scattering by magnetic spheres, *Opt. Soc. Am.* **73**, 765 (1983).

- [39] W. Liu and Y. S. Kivshar, Generalized Kerker effects in nanophotonics and meta-optics [Invited], *Opt. Express* **26**, 13085 (2018).
- [40] H. K. Shamkhi, K. V. Baryshnikova, A. Sayanskiy, P. Kapitanova, P. D. Terekhov, P. Belov, A. Karabchevsky, A. B. Evlyukhin, Y. Kivshar, and A. S. Shalin, Transverse scattering and generalized kerker effects in all-dielectric Mie-resonant metaoptics, *Phys. Rev. Lett.* **122**, 193905 (2019).
- [41] P. D. Terekhov, K. V. Baryshnikova, Y. A. Artemyev, A. Karabchevsky, A. S. Shalin, and A. B. Evlyukhin, Multipolar response of nonspherical silicon nanoparticles in the visible and near-infrared spectral ranges, *Phys. Rev. B* **96**, 035443 (2017).
- [42] A. Doicu and T. Wriedt, Computation of the beam-shape coefficients in the generalized Lorenz-Mie theory by using the translational addition theorem for spherical vector wave functions, *Appl. Opt.* **36**, 2971 (1997).
- [43] Y. L. Geng, X. B. Wu, L. W. Li, and B. R. Guan, Mie scattering by a uniaxial anisotropic sphere, *Phys. Rev. E* **70**, 056609 (2004).
- [44] G. Gouesbet, Localized interpretation to compute all the coefficients g_n^m in the generalized Lorenz-Mie theory, *J. Opt. Soc. Am. A* **7**, 998 (1990).
- [45] J. A. Lock and G. Gouesbet, Rigorous justification to the localized approximation to the beam-shape coefficients in generalized Lorenz-Mie theory. I. On-axis beams, *J. Opt. Soc. Am. A* **11**, 2503 (1994).
- [46] G. Gouesbet and G. Gréhan, *Generalized Lorenz-Mie Theories* (Springer, New York, 2011).
- [47] C. F. Bohren and D. R. Huffman, *Absorption and Scattering of Light by Small Particles* (John Wiley & Sons, New York, 1983).
- [48] J. P. Barton, D. R. Alexander, and S. A. Schaub, Theoretical determination of net radiation force and torque for a spherical particle illuminated by a focused laser beam, *J. Appl. Phys.* **66**, 4594 (1989).
- [49] Z. J. Li, Z. S. Wu, Q. C. Shang, L. Bai, and C. H. Cao, Calculation of radiation forces exerted on a uniaxial anisotropic sphere by an off-axis incident Gaussian beam, *Opt. Express*. **19**, 16044 (2011).